

1

2 Modular strategies for spatial mapping of 3 multi-modal mouse brain data

4 Nicholas J. Tustison¹, Min Chen², Fae N. Kronman³, Jeffrey T. Duda², Clare Gamlin⁴, Mia
5 G. Tustison, Michael Kunst⁴, Rachel Dalley⁴, Staci Sorenson⁴, Quanxin Wang⁴, Lydia Ng⁴,
6 Yongsoo Kim³, and James C. Gee²

7 ¹Department of Radiology and Medical Imaging, University of Virginia, Charlottesville, VA

8 ²Department of Radiology, University of Pennsylvania, Philadelphia, PA

9 ³Department of Neural and Behavioral Sciences, Penn State University, Hershey, PA

10 ⁴Allen Institute for Brain Science, Seattle, WA

11

12 Corresponding authors:

13

14 Nicholas J. Tustison, DSc

15 Department of Radiology and Medical Imaging

16 University of Virginia

17 ntustison@virginia.edu

18

19 James C. Gee, PhD

20 Department of Radiology

21 University of Pennsylvania

22 gee@upenn.edu

²³ **Abstract**

²⁴ Large-scale efforts by the BRAIN Initiative Cell Census Network (BICCN) are generating
²⁵ a comprehensive reference atlas of cell types in the mouse brain. A key challenge in this
²⁶ effort is mapping diverse datasets—acquired with varied imaging, tissue processing, and
²⁷ profiling methods—into shared coordinate frameworks. Here, we present modular mapping
²⁸ pipelines developed using the Advanced Normalization Tools Ecosystem (ANTsX) to align
²⁹ MERFISH spatial transcriptomics and high-resolution fMOST morphology data to the Allen
³⁰ Common Coordinate Framework (CCFv3), and developmental MRI and LSFM data to the
³¹ Developmental CCF (DevCCF). Simultaneously, we introduce two novel methods: 1) a
³² velocity field-based approach for continuous interpolation across developmental timepoints,
³³ and 2) a deep learning framework for automated brain parcellation using minimally annotated
³⁴ and publicly available data. All workflows are open-source and reproducible. We also provide
³⁵ general guidance for selecting appropriate strategies across modalities, enabling researchers
³⁶ to adapt these tools to new data.

³⁷ 1 Introduction

³⁸ Over the past decade, there have been significant advancements in mesoscopic single-cell
³⁹ analysis of the mouse brain. It is now possible to track single neurons¹, observe whole-
⁴⁰ brain developmental changes at cellular resolution², associate brain regions with genetic
⁴¹ composition³, and locally characterize neural connectivity⁴. These scientific achievements have
⁴² been propelled by high-resolution profiling and imaging techniques that enable submicron,
⁴³ multimodal, three-dimensional characterizations of whole mouse brains. Among these are
⁴⁴ micro-optical sectioning tomography^{5,6}, tissue clearing methods^{1,7}, spatial transcriptomics^{8,9},
⁴⁵ and single-cell genomic profiling¹⁰, each offering expanded specificity and resolution for
⁴⁶ cell-level brain analysis.

⁴⁷ Recent efforts by the NIH BRAIN Initiative have mobilized large-scale international col-
⁴⁸ laborations to create a comprehensive reference database of mouse brain structure and
⁴⁹ function. The BRAIN Initiative Cell Census Network has aggregated over 40 multimodal
⁵⁰ datasets from more than 30 research groups¹¹, many of which are registered to standardized
⁵¹ anatomical coordinate systems to support integrated analysis. Among the most widely used
⁵² of these frameworks is the Allen Mouse Brain Common Coordinate Framework (CCFv3)¹².
⁵³ Other CCFs include modality-specific references^{13–15} and developmental atlases^{16,17} that track
⁵⁴ structural change across time.

⁵⁵ 1.1 Mouse brain mapping challenges

⁵⁶ Robust mapping of cell type data into CCFs is essential for integrative analysis of morphology,
⁵⁷ connectivity, and molecular identity. However, each modality poses unique challenges. For
⁵⁸ example, differences in tissue processing, imaging protocols, and anatomical completeness
⁵⁹ often introduce artifacts such as distortion, tearing, holes, and signal dropout^{18–23}. Intensity
⁶⁰ differences and partial representations of anatomy can further complicate alignment. Given
⁶¹ this diversity specialized strategies are often needed to address the unique, modality-specific
⁶² challenges.

⁶³ Existing mapping solutions fall into three broad categories. The first includes integrated

64 processing platforms that provide users with mapped datasets (e.g., Allen Brain Cell Atlas²⁴,
65 Brain Architecture Portal²⁵, OpenBrainMap²⁶, and Image and Multi-Morphology Pipeline²⁷).
66 These offer convenience and high-quality curated data, but limited generalizability and
67 customization. The second category involves highly specialized pipelines tailored to specific
68 modalities such as histology^{28–30}, magnetic resonance imaging (MRI)^{31–33}, microCT^{34,35}, light
69 sheet fluorescence microscopy (LSFM)^{36,37}, fluorescence micro-optical sectioning tomography
70 (fMOST)^{15,38}, and spatial transcriptomics, including multiplexed error-robust fluorescence in
71 situ hybridization (MERFISH)^{39–41}. While effective, these solutions often require extensive
72 engineering effort to adapt to new datasets or modalities. Finally, general-purpose toolkits
73 such as elastix⁴², Slicer3D⁴³, and the Advanced Normalization Tools Ecosystem (ANTsX)⁴⁴
74 have all been applied to mouse brain mapping scenarios (e.g.,⁴⁵). These toolkits support
75 modular workflows that can be flexibly composed from reusable components, offering a
76 powerful alternative to rigid, modality-specific solutions. However, their use often requires
77 familiarity with pipeline modules, parameter tuning, and tool-specific conventions which can
78 limit adoption.

79 Building on this third category, we describe a set of modular, ANTsX-based pipelines
80 specifically tailored for mapping diverse mouse brain data into standardized anatomical
81 frameworks. These include two new pipelines: a velocity field-based interpolation model that
82 potentially enables biologically plausible transformations across developmental timepoints, and
83 a template-based deep learning pipeline for brain extraction and parcellation requiring minimal
84 annotated data. In addition, we include two modular pipelines for aligning multiplexed
85 error-robust fluorescence in situ hybridization (MERFISH) and fMOST datasets to the
86 Allen CCFv3. These workflows were adapted and tailored using ANTsX tools to support
87 collaborative efforts within the BICCN and are now made openly available in a reproducible
88 format. To facilitate broader adoption, we also provide general guidance for customizing
89 these strategies across imaging modalities and data types. We first introduce key components
90 of the ANTsX toolkit, which provide a basis for all of the mapping workflows described here,
91 and then detail the specific contributions made in each pipeline.

92 1.2 The Advanced Normalization Tools Ecosystem (ANTsX)

93 The Advanced Normalization Tools Ecosystem (ANTsX) has been used in a number of
94 applications for mapping mouse brain data as part of core processing steps in various
95 workflows^{30,46–49}, particularly its pairwise, intensity-based image registration capabilities⁵⁰
96 and bias field correction⁵¹. Historically, ANTsX development is based on foundational
97 approaches to image mapping^{52–54}, especially in the human brain, with key contributions such
98 as the Symmetric Normalization (SyN) algorithm⁵⁰. It has been independently evaluated in
99 diverse imaging domains including multi-site brain MRI⁵⁵, pulmonary CT⁵⁶, and multi-modal
100 brain tumor registration⁵⁷.

101 Beyond registration, ANTsX provides functionality for template generation⁵⁸, intensity-based
102 segmentation⁵⁹, preprocessing^{51,60}, and deep learning⁴⁴. It has demonstrated strong perfor-
103 mance in consensus labeling⁶¹, brain tumor segmentation⁶², and cardiac motion estimation⁶³.
104 Built on the Insight Toolkit (ITK)⁶⁴, ANTsX benefits from open-source contributions while
105 supporting continued algorithm evaluation and innovation. In the context of mouse brain
106 data, ANTsX provides a robust platform for developing modular pipelines to map diverse
107 imaging modalities into CCFs. This paper highlights its use across distinct BICCN projects
108 such as spatial transcriptomic data from MERFISH, structural data from fMOST, and
109 multimodal developmental data from LSFM and MRI. We describe both shared infrastructure
110 and targeted strategies adapted to the specific challenges of each modality.

111 1.3 Novel ANTsX-based open-source contributions

112 We introduce two novel contributions to ANTsX developed as part of collabortive efforts in
113 creating the Developmental Common Coordinate Framework (DevCCF)¹⁶. First, we present
114 an open-source velocity field-based interpolation framework for continuous mapping across the
115 sampled embryonic and postnatal stages of the DevCCF atlas¹⁶. This functionality enables
116 biologically plausible interpolation between timepoints via a time-parameterized diffeomorphic
117 velocity model⁶⁵, inspired by previous work⁶⁶. Second, we present a deep learning pipeline for
118 structural parcellation of the mouse brain from multimodal MRI data. This includes two novel

¹¹⁹ components: 1) a template-derived brain extraction model using augmented data from two
¹²⁰ ANTsX-derived template datasets^{67,68}, and 2) a template-derived parcellation model trained
¹²¹ on DevCCF P56 labelings mapped from the AllenCCFv3. This pipeline demonstrates how
¹²² ANTsX tools and public resources can be leveraged to build robust anatomical segmentation
¹²³ pipelines with minimal annotated data. We independently evaluate this framework using a
¹²⁴ longitudinal external dataset⁶⁹, demonstrating generalizability across specimens and imaging
¹²⁵ protocols. All components are openly available through the R and Python ANTsX packages,
¹²⁶ with general-purpose functionality documented in a reproducible, cross-platform tutorial
¹²⁷ (<https://tinyurl.com/antsxtutorial>). Code specific to this manuscript, including scripts to
¹²⁸ reproduce the novel contributions and all associated evaluations, is provided in a dedicated
¹²⁹ repository (<https://github.com/ntustison/ANTsXMouseBrainMapping>). Additional tools for
¹³⁰ mapping spatial transcriptomic (MERFISH) and structural (fMOST) data to the AllenCCFv3
¹³¹ are separately available at (<https://github.com/dontminchenit/CCFAlignmentToolkit>).

132 **2 Results**

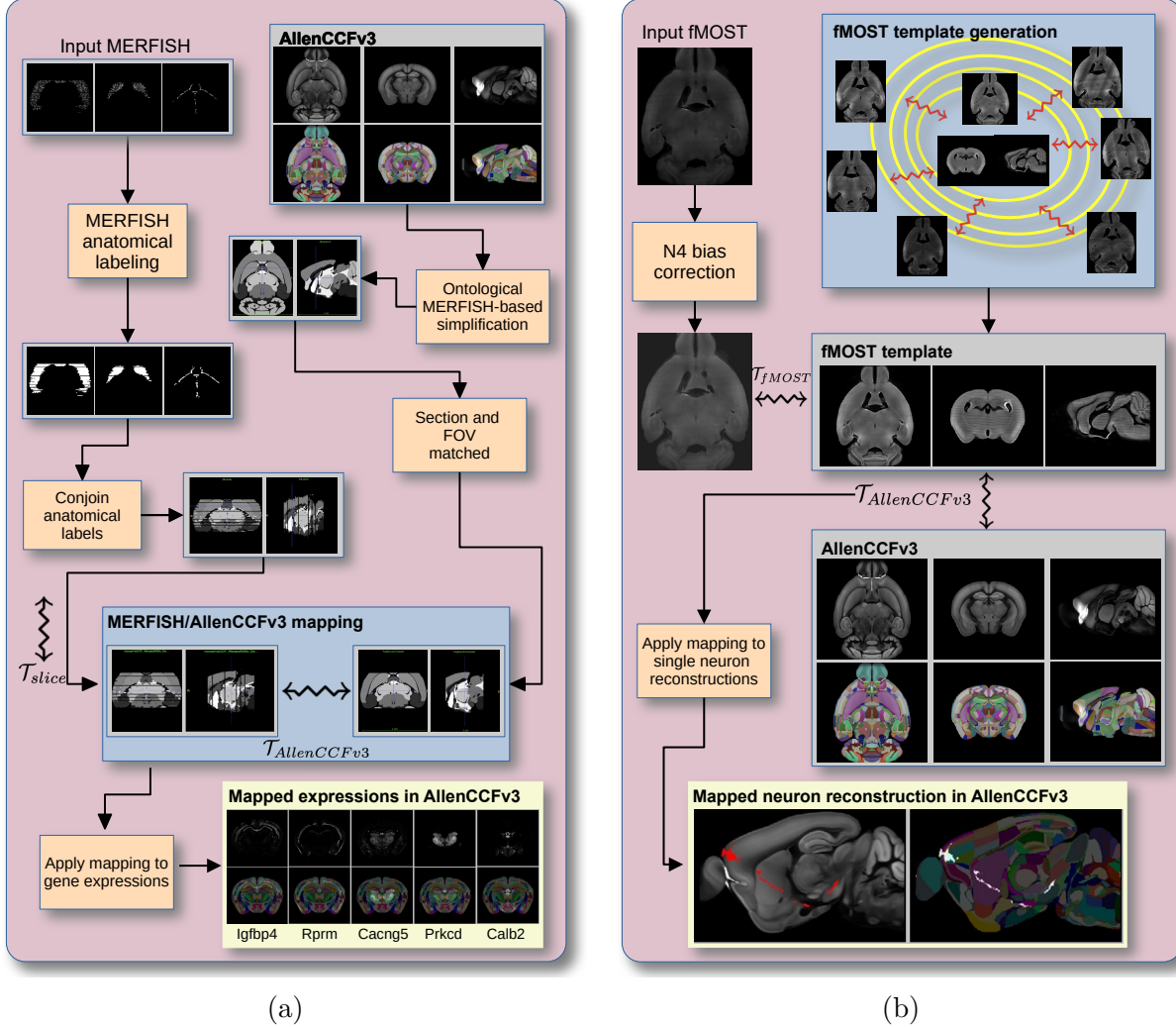


Figure 1: Diagram of the two ANTsX-based pipelines for mapping (a) MERFISH and (b)fMOST data into the space of AllenCCFv3. Each generates the requisite transforms, \mathcal{T} , to map individual images to the CCF.

133 **2.1 AllenCCFv3 brain image mapping**

134 **2.1.1 Mapping multiplexed error-robust fluorescence *in situ* hybridization
(MERFISH) data**

136 **Overview.** The ANTsX framework was used to develop a pipeline for mapping multiplexed
137 error-robust fluorescence *in situ* hybridization (MERFISH) spatial transcriptomic mouse

¹³⁸ data onto the AllenCCFv3 (see Figure 1(a)). This pipeline, used recently in creating
¹³⁹ a high-resolution transcriptomic atlas of the mouse brain⁴⁹, performs mappings by first
¹⁴⁰ generating anatomical labels from tissue related gene expressions in the MERFISH data, and
¹⁴¹ then spatially matching these labels to corresponding anatomical tissue parcellations in the
¹⁴² AllenCCFv3. The pipeline consists of MERFISH data specific preprocessing which includes
¹⁴³ section reconstruction, mapping corresponding anatomical labels between AllenCCFv3 and the
¹⁴⁴ spatial transcriptomic maps of the MERFISH data, and matching MERFISH sections to the
¹⁴⁵ atlas space. Following preprocessing, two main alignment steps were performed: 1) 3-D global
¹⁴⁶ affine mapping and section matching of the AllenCCFv3 into the MERFISH data and 2) 2-D
¹⁴⁷ global and deformable mapping between each MERFISH section and matched AllenCCFv3
¹⁴⁸ section. Mappings learned via each step in the pipeline are preserved and concatenated to
¹⁴⁹ provide point-to-point correspondence between the original MERFISH data and AllenCCFv3,
¹⁵⁰ thus allowing individual gene expressions to be transferred into the AllenCCFv3.

¹⁵¹ **Data.** MERFISH mouse brain data was acquired using a previously detailed procedure⁴⁹.
¹⁵² Briefly, a brain of C57BL/6 mouse was dissected according to standard procedures and placed
¹⁵³ into an optimal cutting temperature (OCT) compound (Sakura FineTek 4583) in which it
¹⁵⁴ was stored at -80°C. The fresh frozen brain was sectioned at 10 μ m on Leica 3050 S cryostats
¹⁵⁵ at intervals of 200 μ m to evenly cover the brain. A set of 500 genes were imaged that had been
¹⁵⁶ carefully chosen to distinguish the ~5200 clusters of our existing RNAseq taxonomy. For
¹⁵⁷ staining the tissue with MERFISH probes, a modified version of instructions provided by the
¹⁵⁸ manufacturer was used⁴⁹. Raw MERSCOPE data were decoded using Vizgen software (v231).
¹⁵⁹ Cells were segmented based on DAPI and PolyT staining using Cellpose^{70,71}. Segmentation
¹⁶⁰ was performed on a median z-plane (fourth out of seven) and cell borders were propagated to
¹⁶¹ z-planes above and below. To assign cluster identity to each cell in the MERFISH dataset,
¹⁶² we mapped the MERFISH cells to the scRNA-seq reference taxonomy.

¹⁶³ **Evaluation.** Alignment of the MERFISH data into the AllenCCFv3 was qualitatively assessed
¹⁶⁴ by an expert anatomist at each iteration of the registration using known correspondence of
¹⁶⁵ gene markers and their associations with the AllenCCFv3. As previously reported⁴⁹, further
¹⁶⁶ assessment of the alignment showed that, of the 554 terminal regions (gray matter only)

¹⁶⁷ in the AllenCCFv3, only seven small subregions were missed from the MERFISH dataset:
¹⁶⁸ frontal pole, layer 1 (FRP1), FRP2/3, FRP5; accessory olfactory bulb, glomerular layer
¹⁶⁹ (AOBgl); accessory olfactory bulb, granular layer (AOBgr); accessory olfactory bulb, mitral
¹⁷⁰ layer (AOBmi); and accessory supraoptic group (ASO).

¹⁷¹ 2.1.2 Mapping fluorescence micro-optical sectioning tomography (fMOST) data

¹⁷² **Overview.** We developed a pipeline for mapping fluorescence micro-optical sectioning
¹⁷³ tomography (fMOST) mouse brain images into the AllenCCFv3 (see Figure 1(b)). The
¹⁷⁴ pipeline is adapted from previously developed frameworks for human brain mapping⁵⁸, and
¹⁷⁵ uses a modality specific (fMOST) average atlas to assist in the image registration and
¹⁷⁶ mapping. This approach has been well validated in human studies^{72–74}, and successfully
¹⁷⁷ used in other mouse data^{12,15,75}. Briefly, we construct an intensity- and shape-based average
¹⁷⁸ fMOST atlas using 30 fMOST images to serve as an intermediate registration target for
¹⁷⁹ mapping fMOST images from individual specimens into the AllenCCFv3. Preprocessing
¹⁸⁰ steps include downsampling to match the $25\mu m$ isotropic AllenCCFv3, acquisition-based
¹⁸¹ stripe artifact removal, and inhomogeneity correction⁵¹. Preprocessing also includes a single
¹⁸² annotation-driven registration to establish a canonical mapping between the fMOST atlas and
¹⁸³ the AllenCCFv3. This step allows us to align expert determined landmarks to accurately map
¹⁸⁴ structures with large morphological differences between the modalities, which are difficult to
¹⁸⁵ address using standard approaches. Once this canonical mapping is established, standard
¹⁸⁶ intensity-based registration is used to align each new fMOST image to the fMOST specific
¹⁸⁷ atlas. This mapping is concatenated with the canonical fMOST atlas-to-AllenCCFv3 mapping
¹⁸⁸ to further map each individual brain into the latter without the need to generate additional
¹⁸⁹ landmarks. Transformations learned through this mapping can be applied to single neuron
¹⁹⁰ reconstructions from the fMOST images to evaluate neuronal distributions across different
¹⁹¹ specimens into the AllenCCFv3 for the purpose of cell census analyses.

¹⁹² **Data.** The high-throughput and high-resolution fluorescence micro-optical sectioning tomog-
¹⁹³ raphy (fMOST)^{76,77} platform was used to image 55 mouse brains containing gene-defined
¹⁹⁴ neuron populations, with sparse transgenic expression^{78,79}. In short, the fMOST imaging

platform results in 3-D images with voxel sizes of $0.35 \times 0.35 \times 1.0 \mu\text{m}^3$ and is a two-channel imaging system where the green channel displays the green fluorescent protein (GFP) labeled neuron morphology and the red channel is used to visualize the counterstained propidium iodide cytoarchitecture. The spatial normalizations described in this work were performed using the red channel, which offered higher tissue contrast for alignment, although other approaches are possible including multi-channel registration.

Evaluation. Evaluation of the canonical fMOST atlas to Allen CCFv3 mapping was performed via quantitative comparison at each step of the registration and qualitative assessment of structural correspondence after alignment by an expert anatomist. Dice values were generated for the following structures: whole brain, 0.99; fimbria, 0.91; habenular commissure, 0.63; posterior choroid plexus, 0.93; anterior choroid plexus, 0.96; optic chiasm, 0.77; caudate putamen, 0.97. Similar qualitative assessment was performed for each fMOST specimen including the corresponding neuron reconstruction data.

2.2 Continuously mapping the DevCCF developmental trajectory with a velocity flow model

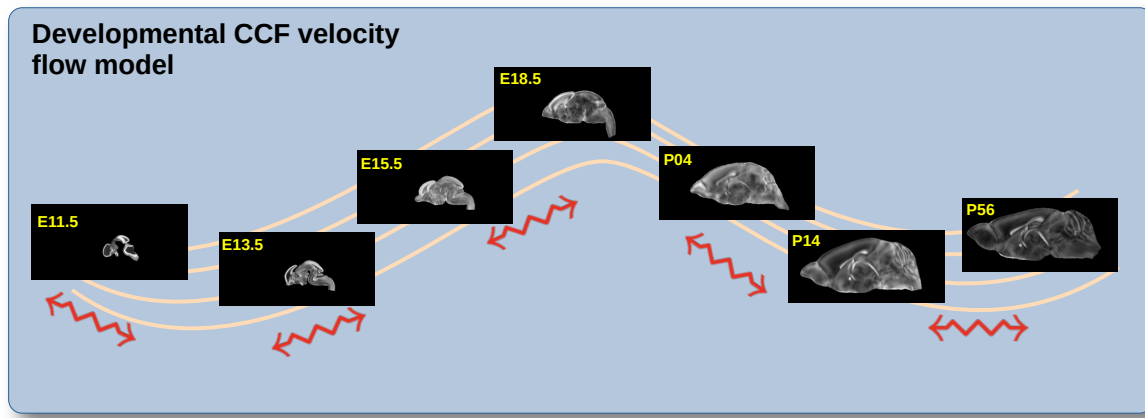


Figure 2: The spatial transformation between any two time points within the continuous DevCCF longitudinal developmental trajectory is available through the use of ANTsX functionality for generating a velocity flow model.

The DevCCF is an openly accessible resource for the mouse brain research community⁸⁰. It

211 consists of multi-modal MRI and LSFM symmetric ANTsX-generated templates⁵⁸ sampling
212 the mouse brain developmental trajectory, specifically the embryonic (E) and postnatal (P)
213 days E11.5, E13.5, E15.5, E18.5 P4, P14, and P56. Each template space includes structural
214 labels defined by a developmental ontology. Its utility is also enhanced by a coordinated
215 construction with AllenCCFv3. Although this work represents a significant contribution, the
216 gaps between time points potentially limit its applicability which could be addressed through
217 the development of the ability to map not only between time points but also within and
218 across time points.

219 To continuously generate transformations between the different stages of the DevCCF atlases,
220 we developed a general velocity flow model approach which we apply to DevCCF-derived
221 data. We also introduce this functionality into both the ANTsR and ANTsPy packages (for
222 the latter, see `ants.fit_time_varying_transform_to_point_sets(...)`) for potential
223 application to this and other analogous scenarios (e.g., modeling the cardiac and respiratory
224 cycles). ANTsX, being built on top of ITK, uses an ITK image data structure for the 4-D
225 velocity field where each voxel contains the x , y , z components of the field at that point.

226 2.2.1 Data

227 Labeled annotations are available as part of the original DevCCF and reside in the space
228 of each developmental template which range in resolution from $31.5 - 50\mu\text{m}$. Across all
229 atlases, the total number of labeled regions exceeds 2500. From these labels, a common set
230 of 26 labels (13 per hemisphere) across all atlases were used for optimization and evaluation.
231 These simplified regions include: terminal hypothalamus, subpallium, pallium, peduncular
232 hypothalamus, prosomere, prosomere, prosomere, midbrain, prepontine hindbrain, pontine
233 hindbrain, pontomedullary hindbrain, medullary hindbrain, and tracts (see Figure 3).

234 Prior to velocity field optimization, all data were rigidly transformed to DevCCF P56 using
235 the centroids of the common label sets. In order to determine the landmark correspondence
236 across DevCCF stages, the multi-metric capabilities of `ants.registration(...)` were used.
237 Instead of performing intensity-based pairwise registration directly on these multi-label
238 images, each label was used to construct a separate fixed and moving image pair resulting in

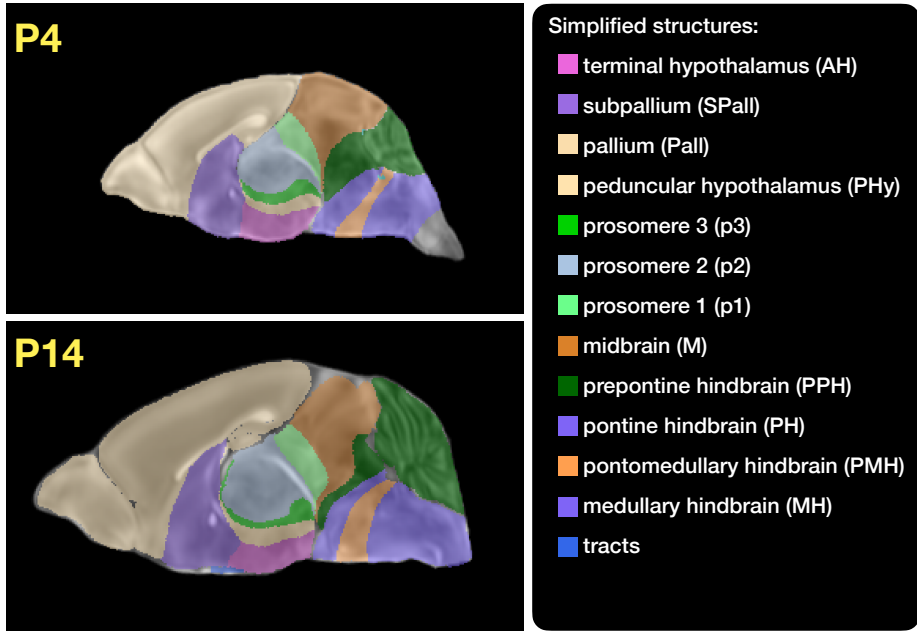


Figure 3: Annotated regions representing common labels across developmental stages which are illustrated for both P4 and P14.

239 a multi-metric registration optimization scenario involving 24 binary image pairs (each label
 240 weighted equally) for optimizing diffeomorphic correspondence between neighboring time
 241 point atlases using the mean squares metric and the symmetric normalization transform⁵⁰.

242 To generate the set of common point sets across all seven developmental atlases, the label
 243 boundaries and whole regions were sampled in the P56 atlas and then propagated to each atlas
 244 using the transformations derived from the pairwise registrations. We selected a sampling
 245 rate of 10% for the contour points and 1% for the regional points for a total number of points
 246 being per atlas being 173303 ($N_{contour} = 98151$ and $N_{region} = 75152$). Regional boundary
 247 points were weighted twice as those of non-boundary points during optimization.

248 2.2.2 Velocity field optimization

249 The velocity field was optimized using the input composed of the seven corresponding point
 250 sets and their associated weight values, the selected number of integration points for the
 251 velocity field ($N = 11$), and the parameters defining the geometry of the spatial dimensions
 252 of the velocity field. Thus, the optimized velocity field described here is of size [256, 182, 360]

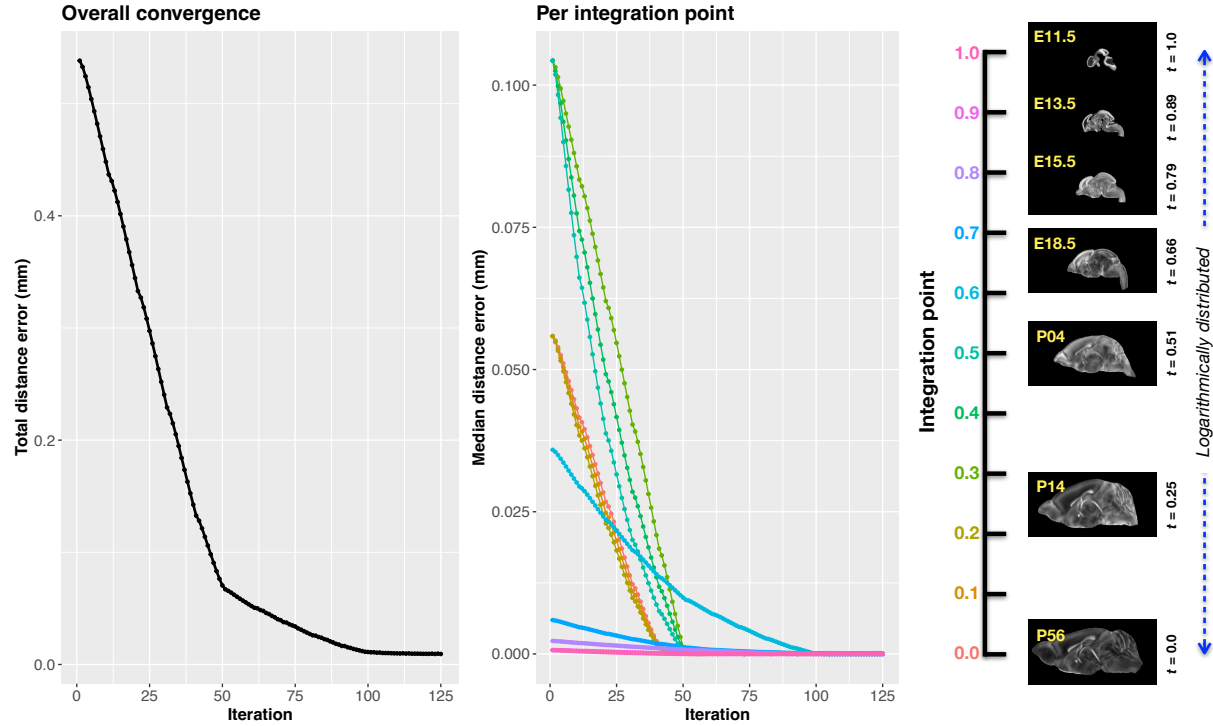


Figure 4: Convergence of the optimization of the velocity field for describing the transformation through the developmental stages from E11.5 through P56. Integration points in diagram on the right are color-coordinated with the center plot and placed in relation to the logarithmically situated temporal placement of the individual DevCCF atlases.

253 (50 μ m isotropic) \times 11 integration points for a total compressed size of a little over 2 GB.
 254 This choice represented weighing the trade-off between tractability, portability, and accuracy.
 255 However, all data and code to reproduce the results described are available in the dedicated
 256 GitHub repository.
 257 The normalized time point scalar value for each atlas/point-set in the temporal domains [0, 1]
 258 was also defined. Given the increasingly larger gaps in the postnatal time point sampling, we
 259 made two adjustments. Based on known mouse brain development, we used 28 days for the
 260 P56 data. We then computed the log transform of the adjusted set of time points prior to
 261 normalization between 0 and 1 (see the right side of Figure 4). This log transform, as part of
 262 the temporal normalization, significantly improves the temporal spacing of data.
 263 The maximum number of iterations was set to 200 with each iteration taking approximately
 264 six minutes on a 2020 iMac (processor, 3.6 GHz 10-Core Intel Core i9; memory, 64 GB 2667
 265 MHz DDR4) At each iteration we looped over the 11 integration points. At each integration

point, the velocity field estimate was updated by warping the two immediately adjacent
 point sets to the integration time point and determining the regularized displacement field
 between the two warped point sets. As with any gradient-based descent algorithm, this
 field was multiplied by a small step size ($\delta = 0.2$) before adding to the current velocity field.
 Convergence is determined by the average displacement error over each of the integration
 points. As can be seen in the left panel of Figure 4, convergence occurred around 125
 iterations when the average displacement error over all integration points is minimized. The
 median displacement error at each of the integration points also trends towards zero but at
 different rates.

2.2.3 The velocity flow transformation model

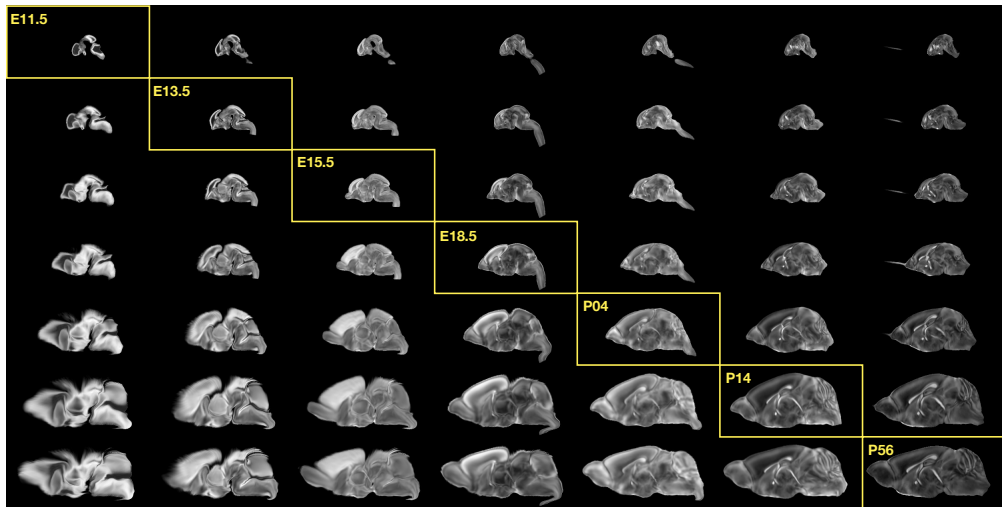


Figure 5: Mid-sagittal visualization of the effects of the transformation model in warping every developmental stage to the time point of every other developmental stage. The original images are located along the diagonal. Columns correspond to the warped original image whereas the rows represent the reference space to which each image is warped.

Once optimized, the resulting velocity field can be used to generate the deformable transform
 between any two continuous points within the time interval bounded by E11.5 and P56.
 As a demonstration, in Figure 5, we transform each atlas to the space of every other atlas
 using the DevCCF transform model. Additionally, one can use this transformation model to
 construct virtual templates in the temporal gaps of the DevCCF. Given an arbitrarily chosen
 time point within the normalized time point interval, the existing adjacent DevCCF atlases

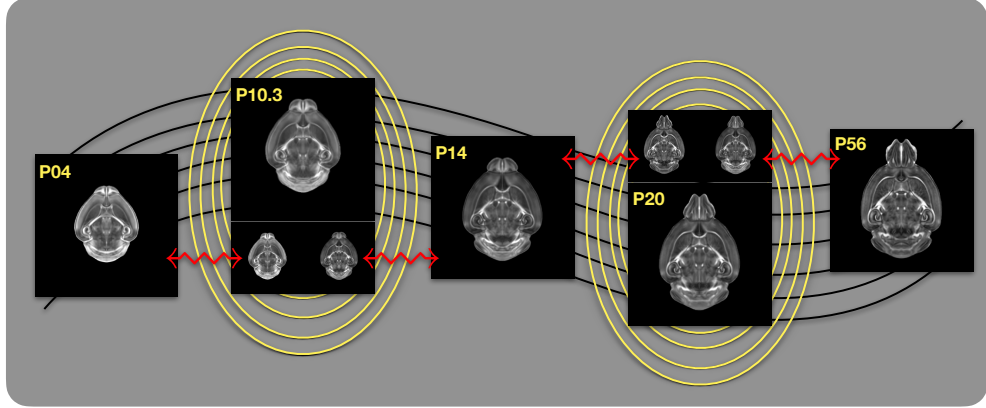


Figure 6: Illustration of the use of the velocity flow model for creating virtual templates at continuous time points not represented in one of the existing DevCCF time points. For example, FA templates at time point P10.3 and P20 can be generated by warping the existing temporally adjacent developmental templates to the target time point and using those images in the ANTsX template building process.

282 on either chronological side can be warped to the desired time point. A subsequent call to
 283 one of the ANTsX template building functions then permits the construction of the template
 284 at that time point. In Figure 6, we illustrate the use of the DevCCF velocity flow model for
 285 generating two such virtual templates for two arbitrary time points. Note that both of these
 286 usage examples can be found in the GitHub repository previously given.

287 2.3 Automated structural parcellations of the mouse brain

288 Brain parcellation strategies for the mouse brain are pivotal for understanding the complex
 289 organization and function of murine nervous system⁸¹. By dividing the brain into distinct
 290 regions based on anatomical, physiological, or functional characteristics, researchers can
 291 investigate specific areas in isolation and identify their roles in various behaviors and processes.
 292 For example, such parcellation schemes can help elucidate the spatial distribution of gene
 293 expression patterns⁸² as well as identify functional regions involved in specific cognitive
 294 tasks⁸³.

295 Although deep learning techniques have been used to develop useful parcellation tools for
 296 human brain research (e.g., SynthSeg⁸⁴, ANTsXNet⁴⁴), analogous development for the mouse
 297 brain is limited. In addition, mouse data is often characterized by unique imaging issues

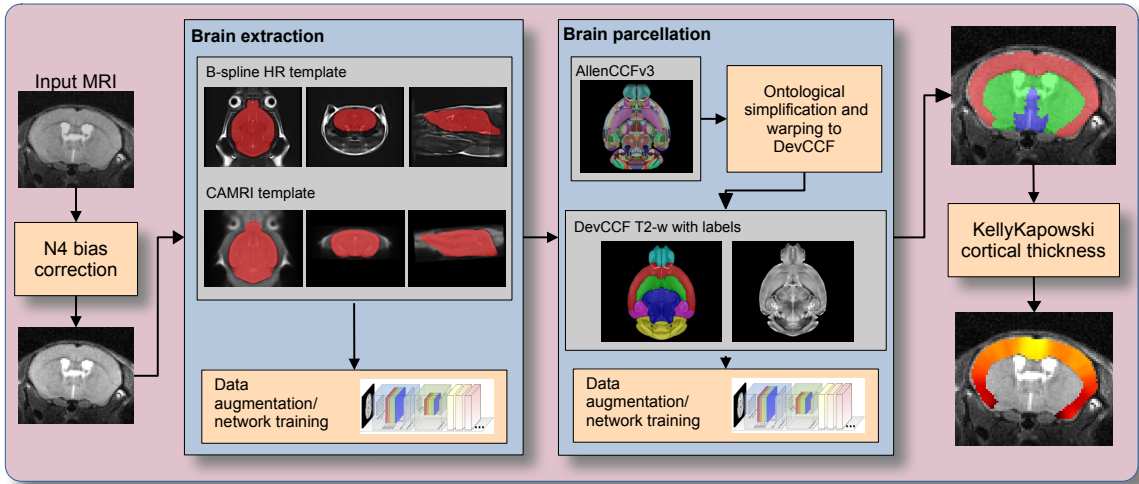


Figure 7: The mouse brain cortical parcellation pipeline integrating two deep learning components for brain extraction and brain parcellation prior to estimating cortical labels. Both deep learning networks rely heavily on aggressive data augmentation on templates built from open data and provide an outline for further refinement and creating alternative parcellations for tailored research objectives. Possible applications include voxelwise cortical thickness measurements.

such as extreme anisotropic sampling which are often in sharp contrast to the high resolution template-based resources available within the community, e.g., AllenCCFv3 and DevCCF. We demonstrate how one can use the ANTsX tools to develop a complete mouse brain structural morphology pipeline as illustrated in Figure 7 and detailed below.

2.3.1 Few-shot mouse brain extraction network

In order to create a generalized mouse brain extraction network, we built whole-head templates from two publicly available datasets. The Center for Animal MRI (CAMRI) dataset⁶⁷ from the University of North Carolina at Chapel Hill consists of 16 T2-w MRI volumes of voxel resolution $0.16 \times 0.16 \times 0.16 mm^3$. The second high-resolution dataset⁶⁸ comprises 88 specimens each with three spatially aligned canonical views with in-plane resolution of $0.08 \times 0.08 mm^2$ with a slice thickness of $0.5 mm$. These three orthogonal views were used to reconstruct a single high-resolution volume per subject using a B-spline fitting algorithm available in ANTsX⁸⁵.

From these two datasets, two ANTsX templates⁵⁸ were generated. Bias field simulation,

312 intensity histogram warping, noise simulation, random translation and warping, and random
313 anisotropic resampling in the three canonical directions were used for data augmentation
314 in training an initial T2-w brain extraction network. This network was posted and the
315 corresponding functionality was immediately made available within ANTsXNet, similar to
316 our previous contributions to the community.

317 User interest led to a GitHub inquiry regarding possible study-specific improvements (<https://github.com/ANTsX/ANTsPyNet/issues/133>). This interaction led to the offering of a
318 user-made third template and extracted brain mask generated from T2-w ex-vivo data with
319 isotropic spacing of 0.08 mm in each voxel dimension. This third template, in conjunction
320 with the other two, were used with the same aggressive data augmentation to refine the
321 network weights which were subsequently posted and made available through ANTsPyNet
322 using the function `antspynet.mouse_brain_extraction(...)`.

324 2.3.2 Single-shot mouse brain parcellation network

325 AllenCCFv3 and its hierarchical ontological labeling, along with the DevCCF, provides the
326 necessary data for developing a tailored structural parcellation network for multi-modal
327 imaging. The `allensdk` Python library permits the creation of any gross parcellation based
328 on the AllenCCFv3 ontology. Specifically, using `allensdk` we coalesced the labels to the
329 following six major structures: cerebral cortex, cerebral nuclei, brain stem, cerebellum, main
330 olfactory bulb, and hippocampal formation. This labeling was mapped to the P56 component
331 of the DevCCF for use with the T2-w template component.

332 The T2-w P56 DevCCF and labelings, in conjunction with the data augmentation
333 described previously for brain extraction, were used to train the proposed brain
334 parcellation network. This is available in ANTsXNet (e.g. in ANTsPyNet using
335 `antspynet.mouse_brain_parcellation(...)`). Note that other brain parcellation net-
336 works have also been trained using alternative regions and parcellation schemes and are
337 available in the same ANTsXNet functionality. One usage note is that the data augmentation
338 used to train the network permits a learned interpolation in 0.08 mm isotropic space. Since
339 the training data is isotropic and data augmentation includes downsampling in the canonical

340 directions, each of the two networks learns mouse brain-specific interpolation such that
 341 one can perform prediction on thick-sliced images, as, for example, in these evaluation
 342 data, and return isotropic probability and thickness maps (a choice available to the user).
 343 This permits robust cortical thickness estimation even in the case of anisotropic data (see
 344 `antspynet.mouse_cortical_thickness(...)`).

345 2.3.3 Evaluation

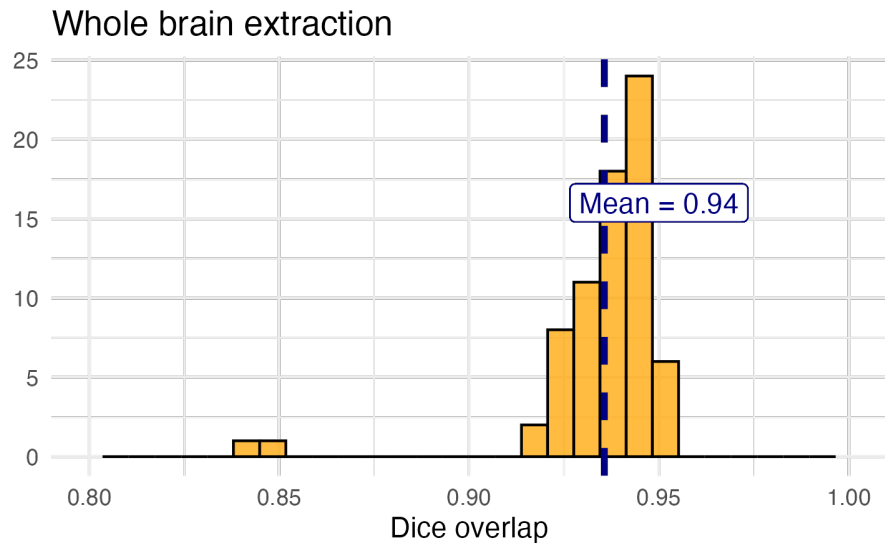
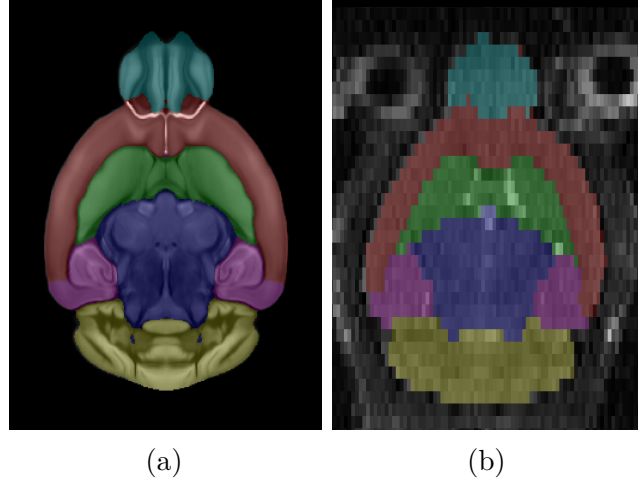


Figure 8: Evaluation of the ANTsX mouse brain extraction on an independent, publicly available dataset consisting of 12 specimens \times 7 time points = 84 total images. Dice overlap comparisons with the user-generated brain masks provide good agreement with the automated results from the brain extraction network.

346 For evaluation, we used an additional publicly available dataset⁶⁹ that is completely indepen-
 347 dent from the data used in training the brain extraction and parcellation networks. Data
 348 includes 12 specimens each imaged at seven time points (Day 0, Day 3, Week 1, Week 4,
 349 Week 8, Week 20) with in-house-generated brain masks for a total of 84 images. Spacing is
 350 anistropic with an in-plane resolution of $0.1 \times 0.1 mm^2$ and a slice thickness of $0.5 mm$.

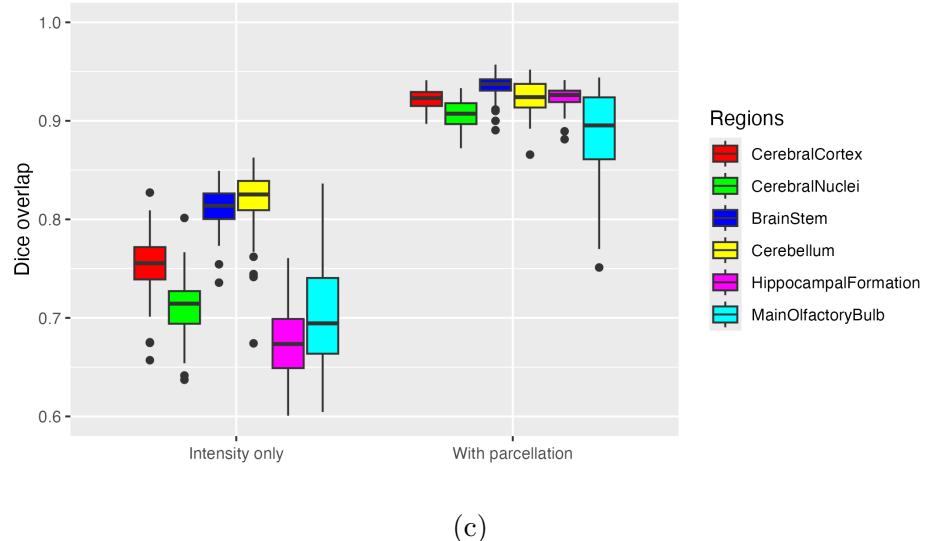
 351 Figure 8 summarizes the whole brain overlap between the provided segmentations for all
 352 84 images and the results of applying the proposed network. Also, since mapping to the
 353 AllenCCFv3 atlas is crucial for many mouse studies, we demonstrate the utility of the second



(a)

(b)

Normalization to AllenCCFv3



(c)

Figure 9: Evaluation of the ANTsX mouse brain parcellation on the same dataset. (a) T2-w DevCCF P56 with the described parcellation consisting of the cerebral cortex, nuclei, brain stem, cerebellum, main olfactory bulb, and hippocampal formation. (b) Sample subject (NR5 Day 0) with the proposed deep learning-based segmentation. (c) Dice overlap for comparing the regional alignments between registration using intensity information only and using intensity with the given parcellation scheme.

³⁵⁴ network by leveraging the labeled regions to perform anatomically-explicit alignment using
³⁵⁵ ANTsX multi-component registration instead of intensity-only registration. For these data,
³⁵⁶ the whole brain extraction demonstrates excellent performance across the large age range.
³⁵⁷ And although the intensity-only image registration provides adequate alignment, intensity
³⁵⁸ with the regional parcellations significantly improves those measures.

³⁵⁹ **3 Discussion**

³⁶⁰ The diverse mouse brain cell type profiles gathered through BICCN and associated efforts
³⁶¹ provide a rich multi-modal resource to the research community. However, despite significant
³⁶² progress, optimal leveraging of these valuable resources remains an ongoing challenge. A
³⁶³ central component to data integration is accurately mapping novel cell type data into
³⁶⁴ common coordinate frameworks (CCFs) for subsequent processing and analysis. To meet
³⁶⁵ these needs, tools for mapping mouse brain data must be both broadly accessible and
³⁶⁶ capable of addressing challenges unique to each modality. In this work, we described modular
³⁶⁷ ANTsX-based pipelines developed to support three distinct BICCN efforts encompassing
³⁶⁸ spatial transcriptomic, morphological, and developmental data. We demonstrated how a
³⁶⁹ flexible image analysis toolkit like ANTsX can be tailored to address specific modality-driven
³⁷⁰ constraints by leveraging reusable, validated components.

³⁷¹ The MERFISH mapping pipeline illustrates how ANTsX tools can be adapted to accommodate
³⁷² high-resolution spatial transcriptomic data. While the general mapping strategy is applicable
³⁷³ to other sectioned histological data, the pipeline includes specific adjustments for known
³⁷⁴ anatomical and imaging artifacts present in MERFISH datasets. As such, this example
³⁷⁵ demonstrates how general-purpose tools can be customized to meet the requirements of highly
³⁷⁶ specialized data types.

³⁷⁷ The fMOST mapping pipeline was developed with the intention of broader applicability.
³⁷⁸ Built primarily from existing ANTsX preprocessing and registration modules, this pipeline
³⁷⁹ introduces an fMOST-specific intermediate atlas to facilitate consistent mappings to the
³⁸⁰ AllenCCFv3. The use of a canonical fMOST atlas reduces the need for repeated manual
³⁸¹ alignment across new datasets, and the resulting transformations can be directly applied to
³⁸² associated single-neuron reconstructions. This supports integrative morphological analysis
³⁸³ across specimens using a common coordinate system.

³⁸⁴ For developmental data, we introduced a velocity field-based model for continuous interpo-
³⁸⁵ lation between discrete DevCCF timepoints. Although the DevCCF substantially expands
³⁸⁶ coverage of developmental stages relative to prior atlases, temporal gaps remain. The velocity

387 model enables spatio-temporal transformations within the full developmental interval and
388 supports the generation of virtual templates at unsampled ages. This functionality is built
389 using ANTsX components for velocity field optimization and integration, and offers a novel
390 mechanism for interpolating across the non-linear developmental trajectory of the mouse brain.
391 Such interpolation has potential utility for both anatomical harmonization and longitudinal
392 analyses.

393 We also introduced a template-based deep learning pipeline for mouse brain extraction and
394 parcellation using aggressive data augmentation. This approach is designed to reduce the
395 reliance on large annotated training datasets, which remain limited in the mouse imaging
396 domain. Evaluation on independent data demonstrates promising generalization, though
397 further refinement will be necessary. As with our human-based ANTsX pipelines, failure
398 cases can be manually corrected and recycled into future training cycles. Community
399 contributions are welcomed and encouraged, providing a pathway for continuous improvement
400 and adaptation to new datasets.

401 The ANTsX ecosystem offers a powerful foundation for constructing scalable, reproducible
402 pipelines for mouse brain data analysis. Its modular design and multi-platform support enable
403 researchers to develop customized workflows without extensive new software development.
404 The widespread use of ANTsX components across the neuroimaging community attests to its
405 utility and reliability. As a continuation of the BICCN program, ANTsX is well positioned to
406 support the goals of the BRAIN Initiative Cell Atlas Network (BICAN) and future efforts to
407 extend these mapping strategies to the human brain.

408 **4 Methods**

409 The following methods are all available as part of the ANTsX ecosystem with analogous
410 elements existing in both ANTsR (ANTs in R) and ANTsPy (ANTs in Python), underpinned by
411 a shared ANTs/ITK C++ core. Most development for the work described was performed using
412 ANTsPy. For equivalent functionality in ANTsR, we refer the reader to the comprehensive
413 ANTsX tutorial: <https://tinyurl.com/antsxtutorial>.

414 **4.1 General ANTsX utilities**

415 Although focused on distinct data types, the three pipelines presented in this work share
416 common components that address general challenges in mapping mouse brain data. These
417 include correcting image intensity artifacts, denoising, spatial registration, template generation,
418 and visualization. Table 1 provides a concise summary of the relevant ANTsX functionality.

419 **Preprocessing: bias field correction and denoising.** Standard preprocessing steps in
420 mouse brain imaging include correcting for spatial intensity inhomogeneities and reducing
421 image noise, both of which can impact registration accuracy and downstream analysis. ANTsX
422 provides implementations of widely used methods for these tasks. The N4 bias field correction
423 algorithm⁵¹, originally developed in ANTs and contributed to ITK, mitigates artifactual, low-
424 frequency intensity variation and is accessible via `ants.n4_bias_field_correction(...)`.
425 Patch-based denoising⁶⁰ has been implemented as `ants.denoise_image(...)`.

426 **Image registration.** ANTsX includes a robust and flexible framework for pairwise
427 and groupwise image registration⁸⁶. At its core is the SyN algorithm⁵⁰, a symmetric
428 diffeomorphic model with optional B-spline regularization⁶⁶. In ANTsPy, registration
429 is performed via `ants.registration(...)` using preconfigured parameter sets (e.g.,
430 `antsRegistrationSyNQuick[s]`, `antsRegistrationSyN[s]`) suitable for different imaging
431 modalities and levels of computational demand. Resulting transformations can be applied to
432 new images with `ants.apply_transforms(...)`.

433 **Template generation.** ANTsX supports population-based template generation through
434 iterative pairwise registration to an evolving estimate of the mean shape and intensity

Table 1: Sampling of ANTsX functionality

<i>ANTsPy: Preprocessing</i>	
bias field correction	<code>n4_bias_field_correction(...)</code>
image denoising	<code>denoise_image(...)</code>
<i>ANTsPy: Registration</i>	
image registration	<code>registration(...)</code>
image transformation	<code>apply_transforms(...)</code>
template generation	<code>build_template(...)</code>
landmark registration	<code>fit_transform_to_paired_points(...)</code>
time-varying landmark reg.	<code>fit_time_varying_transform_to_point_sets(...)</code>
integrate velocity field	<code>integrate_velocity_field(...)</code>
invert displacement field	<code>invert_displacement_field(...)</code>
<i>ANTsPy: Segmentation</i>	
MRF-based segmentation	<code>atropos(...)</code>
Joint label fusion	<code>joint_label_fusion(...)</code>
diffeomorphic thickness	<code>kelly_kapowski(...)</code>
<i>ANTsPy: Miscellaneous</i>	
Regional intensity statistics	<code>label_stats(...)</code>
Regional shape measures	<code>label_geometry_measures(...)</code>
B-spline approximation	<code>fit_bspline_object_to_scattered_data(...)</code>
Visualize images and overlays	<code>plot(...)</code>
<i>ANTsPyNet: Mouse-specific</i>	
brain extraction	<code>mouse_brain_extraction(...modality="t2"...)</code>
brain parcellation	<code>mouse_brain_parcellation(...)</code>
cortical thickness	<code>mouse_cortical_thickness(...)</code>
super resolution	<code>mouse_histology_super_resolution(...)</code>

ANTsX provides state-of-the-art functionality for processing biomedical image data. Such tools, including deep learning networks, support a variety of mapping-related tasks. A more comprehensive listing of ANTsX tools with self-contained R and Python examples is provided as a gist page on GitHub (<https://tinyurl.com/antsxtutorial>).

435 reference space across subjects⁵⁸. This functionality was used in generating the DevCCF
436 templates¹⁶. The procedure, implemented as `ants.build_template(...)`, produces average
437 images in both shape and intensity by aligning all inputs to a common evolving template.

438 **Visualization.** To support visual inspection and quality control, ANTsPy provides flexible
439 image visualization with `ants.plot(...)`. This function enables multi-slice and multi-
440 orientation rendering with optional overlays and label maps.

441 4.2 Mapping fMOST data to AllenCCFv3

442 **Preprocessing.** Mapping fMOST data into the AllenCCFv3 presents unique challenges due
443 to its native ultra-high resolution and imaging artifacts common to the fMOST modality.
444 Each fMOST image can exceed a terabyte in size, with spatial resolutions far exceeding
445 those of the AllenCCFv3 ($25\ \mu m$ isotropic). To reduce computational burden and prevent
446 resolution mismatch, each fMOST image is downsampled using cubic B-spline interpolation
447 via `ants.resample_image(...)` to match the template resolution.

448 Stripe artifacts (i.e., periodic intensity distortions caused by nonuniform sectioning or illumina-
449 nation) are common in fMOST and can mislead deformable registration algorithms. These
450 were removed using a custom 3D notch filter (`remove_stripe_artifact(...)`) implemented
451 in the `CCFAlignmentToolkit` using SciPy frequency domain filtering. The filter targets
452 dominant stripe frequencies along a user-specified axis in the Fourier domain. In addition,
453 intensity inhomogeneity across sections, often arising from variable staining or illumination,
454 was corrected using N4 bias field correction.

455 **Template-based spatial normalization.** To facilitate reproducible mapping, we first
456 constructed a contralaterally symmetric average template from 30 fMOST brains and their
457 mirrored counterparts using ANTsX template-building tools. Because the AllenCCFv3 and
458 fMOST data differ substantially in both intensity contrast and morphology, direct deformable
459 registration between individual fMOST brains and the AllenCCFv3 was insufficiently robust.
460 Instead, we performed a one-time expert-guided label-driven registration between the average
461 fMOST template and AllenCCFv3. This involved sequential alignment of seven manually

462 selected anatomical regions: 1) brain mask/ventricles, 2) caudate/putamen, 3) fimbria, 4)
463 posterior choroid plexus, 5) optic chiasm, 6) anterior choroid plexus, and 7) habenular
464 commissure which were prioritized to enable coarse-to-fine correction of shape differences.
465 Once established, this fMOST-template-to-AllenCCFv3 transform was reused for all subse-
466 quent specimens. Each new fMOST brain was then registered to the average fMOST template
467 using intensity-based registration, followed by concatenation of transforms to produce the
468 final mapping into AllenCCFv3 space.

469 **Mapping neuron projections.** A key advantage of fMOST imaging is its ability to
470 support single neuron projection reconstruction across the entire brain⁷⁹. Because these
471 reconstructions are stored as 3D point sets aligned to the original fMOST volume, we applied
472 the same composite transform used for image alignment to the point data using ANTsX
473 functionality. This enables seamless integration of cellular morphology data into AllenCCFv3
474 space, facilitating comparative analyses across specimens.

475 4.3 Mapping MERFISH data to AllenCCFv3

476 **Preprocessing.** MERFISH data are acquired as a series of 2D tissue sections, each comprising
477 spatially localized gene expression measurements at subcellular resolution. To enable 3D
478 mapping to the AllenCCFv3, we first constructed anatomical reference images by aggregating
479 the number of detected transcripts per voxel across all probes within each section. These 2D
480 projections were resampled to a resolution of $10 \mu m \times 10 \mu m$ to match the in-plane resolution
481 of the AllenCCFv3.

482 Sections were coarsely aligned using manually annotated dorsal and ventral midline points,
483 allowing initial volumetric reconstruction. However, anatomical fidelity remained limited by
484 variation in section orientation, spacing, and tissue loss. To further constrain alignment and
485 enable deformable registration, we derived region-level anatomical labels directly from the
486 gene expression data.

487 **Label creation.** We assigned each detected cell to one of 15 coarse anatomical regions (e.g.,
488 hippocampus, cortex, striatum—using transcriptomic similarity to scRNA) seq reference

489 data. These assignments were aggregated across spatial grids to produce probabilistic label
490 maps for each section. To ensure full regional coverage, morphological dilation was applied to
491 fill gaps between sparsely distributed cells. Finer-resolution structures (e.g., cortical layers,
492 habenula) were similarly labeled using marker gene enrichment and spatial constraints. This
493 dual-level labeling (i.e., coarse and fine) allowed us to construct a robust anatomical scaffold
494 in the MERFISH coordinate system that could be matched to AllenCCFv3 annotations.

495 **Section matching via global alignment.** A major challenge was compensating for oblique
496 cutting angles and non-uniform section thickness, which distort the anatomical shape and
497 spacing of the reconstructed volume. Rather than directly warping the MERFISH data into
498 atlas space, we globally aligned the AllenCCFv3 to the MERFISH coordinate system. This
499 was done via an affine transformation followed by resampling of AllenCCFv3 sections to match
500 the number and orientation of MERFISH sections. This approach minimizes interpolation
501 artifacts in the MERFISH data and facilitates one-to-one section matching.

502 **Landmark-driven deformable alignment.** We used a 2.5D approach for fine alignment of
503 individual sections. In each MERFISH slice, deformable registration was driven by sequential
504 alignment of anatomical landmarks between the label maps derived from MERFISH and
505 AllenCCFv3. A total of nine regions—including isocortical layers 2/3, 5, and 6, the striatum,
506 hippocampus, thalamus, and medial/lateral habenula—were registered in an empirically
507 determined order. After each round, anatomical alignment was visually assessed by an expert,
508 and the next structure was selected to maximize improvement in the remaining misaligned
509 regions.

510 The final transform for each section combined the global affine alignment and the per-structure
511 deformable registrations. These were concatenated to generate a 3D mapping from the original
512 MERFISH space to the AllenCCFv3 coordinate system. Once established, the composite
513 mapping enables direct transfer of gene-level and cell-type data from MERFISH into atlas
514 space, allowing integration with other imaging and annotation datasets.

515 **4.4 DevCCF velocity flow transformation model**

516 The Developmental Common Coordinate Framework (DevCCF)¹⁶ provides a discrete set of
517 age-specific templates that temporally sample the developmental trajectory. To model this
518 biological progression more continuously, we introduce a velocity flow-based paradigm for
519 inferring diffeomorphic transformations between developmental stages. This enables anatom-
520 ically plausible estimation of intermediate templates or mappings at arbitrary timepoints
521 between the E11.5 and P56 endpoints of the DevCCF. Our approach builds on established
522 insights from time-varying diffeomorphic registration⁶⁵, where a velocity field governs the
523 smooth deformation of anatomical structures over time. Importantly, the framework is
524 extensible and can naturally accommodate additional timepoints for the potential expansion
525 of the DevCCF.

526 **Point sampling and region correspondence.** We first coalesced the anatomical labels
527 across the seven DevCCF templates (E11.5, E13.5, E15.5, E18.5, P4, P14, P56) into 26
528 common structures that could be consistently identified across development. These include
529 major brain regions such as the cortex, cerebellum, hippocampus, midbrain, and ventricles.
530 For each successive pair of templates, we performed multi-label deformable registration
531 using ANTsX to generate forward and inverse transforms between anatomical label volumes.
532 From the P56 space, we randomly sampled approximately 1e6 points within and along the
533 boundaries of each labeled region and propagated them through each pairwise mapping step
534 (e.g., P56 → P14, P14 → P4, ..., E13.5 → E11.5). This procedure created time-indexed
535 point sets tracing the spatial evolution of each region.

536 **Velocity field fitting.** Using these point sets, we fit a continuous velocity field over
537 developmental time using a generalized B-spline scattered data approximation method⁸⁵.
538 The field was parameterized over a log-scaled time axis to ensure finer temporal resolution
539 during early embryonic stages, where morphological changes are most rapid. Optimization
540 proceeded for approximately 125 iterations, minimizing the average Euclidean norm between
541 transformed points at each step. Ten integration points were used to ensure numerical
542 stability. The result is a smooth, differentiable vector field that defines a diffeomorphic
543 transform between any two timepoints within the template range.

544 **Applications and availability.** This velocity model can be used to estimate spatial transfor-
545 mations between any pair of developmental stages—even those for which no empirical template
546 exists—allowing researchers to create interpolated atlases, align new datasets, or measure con-
547 tinuous structural changes. It also enables developmental alignment of multi-modal data (e.g.,
548 MRI to LSFM) by acting as a unifying spatiotemporal scaffold. The underlying components
549 for velocity field fitting and integration are implemented in ITK, and the complete workflow
550 is accessible in both ANTsPy (`ants.fit_time_varying_transform_to_point_sets(...)`)
551 and ANTsR. In addition the availability of the DevCCF use case, self-contained examples
552 and usage tutorials are provided in our public codebase.

553 4.5 Automated brain extraction and parcellation with ANTsXNet

554 To support template-based deep learning approaches for structural brain extraction and par-
555 cellation, we implemented dedicated pipelines using the ANTsXNet framework. ANTsXNet
556 comprises open-source deep learning libraries in both Python (ANTsPyNet) and R (ANTsR-
557 Net) that interface with the broader ANTsX ecosystem and are built on TensorFlow/Keras.
558 Our mouse brain pipelines mirror existing ANTsXNet tools for human imaging but are
559 adapted for species-specific anatomical variation, lower SNR, and heterogeneous acquisition
560 protocols.

561 4.5.1 Deep learning training setup

562 All networks were implemented in ANTsPyNet using standard 3D U-net architectures⁸⁷
563 previously employed in previously published work⁴⁴. Training was performed on an NVIDIA
564 DGX system (4 × Tesla V100 GPUs, 256 GB RAM). Model weights and preprocessing
565 routines are shared across ANTsPyNet and ANTsRNet to ensure reproducibility and lan-
566 guage portability. For both published and unpublished trained networks available through
567 ANTsXNet, all training scripts and data augmentation generators are publicly available at
568 <https://github.com/ntustison/ANTsXNetTraining>.

569 **Data augmentation.** Robust data augmentation was critical to generalization across

570 scanners, contrast types, and resolutions. We applied both intensity- and shape-based
571 augmentation strategies:

572 • *Intensity augmentations:*

- 573 – Gaussian, Poisson, and salt-and-pepper noise:
574 `ants.add_noise_to_image(...)`
- 575 – Simulated intensity inhomogeneity via bias field modeling⁵¹:
576 `antspynet.simulate_bias_field(...)`
- 577 – Histogram warping to simulate contrast variation⁸⁸:
578 `antspynet.histogram_warp_image_intensities(...)`

579 • *Shape augmentations:*

- 580 – Random nonlinear deformations and affine transforms:
581 `antspynet.randomly_transform_image_data(...)`
- 582 – Anisotropic resampling across axial, sagittal, and coronal planes:
583 `ants.resample_image(...)`

584 **4.5.2 Brain extraction**

585 We originally trained a mouse-specific brain extraction model on two manually masked
586 T2-weighted templates, generated from public datasets^{67,68}. One of the templates was
587 constructed from orthogonal 2D acquisitions using B-spline-based volumetric synthesis
588 via `ants.fit_bspline_object_to_scattered_data(...)`. Normalized gradient magnitude
589 was used as a weighting function to emphasize boundaries during reconstruction⁸⁵.

590 This training strategy provides strong spatial priors despite limited data by leveraging
591 high-quality template images and aggressive augmentation to mimic population variability.
592 During the development of this work, the network was further refined through community
593 engagement. A user from a U.S.-based research institute applied the publicly available (but
594 then unpublished) brain extraction tool to their own mouse MRI dataset. Based on feedback
595 and iterative collaboration with the ANTsX team, the model was retrained and improved to

596 better generalize to additional imaging contexts. This reflects our broader commitment to
597 community-driven development and responsiveness to user needs across diverse mouse brain
598 imaging scenarios.

599 The final trained network is available via ANTsXNet through the function
600 `antspynet.mouse_brain_extraction(...)`. Additionally, both template/mask pairs are
601 accessible via ANTsXNet. For example, one such image pair is available via:

- Template:

```
antspynet.get_antsxnet_data("bsplineT2MouseTemplate")
```

- Brain mask:

```
antspynet.get_antsxnet_data("bsplineT2MouseTemplateBrainMask")
```

606 4.5.3 Brain parcellation

607 For brain parcellation, we trained a 3D U-net model using the DevCCF P56 T2-weighted
608 template and anatomical segmentations derived from AllenCCFv3. This template-based
609 training strategy enables the model to produce accurate, multi-region parcellations without
610 requiring large-scale annotated subject data.

611 To normalize intensity across specimens, input images were preprocessed using rank-based
612 intensity normalization (`ants.rank_intensity(...)`). Spatial harmonization was achieved
613 through affine and deformable alignment of each extracted brain to the P56 template prior
614 to inference. In addition to the normalized image input, the network also receives prior
615 probability maps derived from the atlas segmentations, providing additional spatial context.

616 This general parcellation deep learning framework has also been applied in collaboration
617 with other groups pursuing related but distinct projects. In one case, a model variant
618 was adapted for T2-weighted MRI using an alternative anatomical labeling scheme; in
619 another, a separate model was developed for serial two-photon tomography (STPT) with
620 a different parcellation set. All three models are accessible through a shared interface
621 in ANTsXNet: `antspynet.mouse_brain_parcellation(...)`. Ongoing work is further
622 extending this approach to embryonic mouse brain data. These independent efforts reflect

623 broader community interest in adaptable parcellation tools and reinforce the utility of
624 ANTsXNet as a platform for reproducible, extensible deep learning workflows.

625 **4.5.4 Evaluation and reuse**

626 To assess model generalizability, both the brain extraction and parcellation networks were
627 evaluated on an independent longitudinal dataset comprising multiple imaging sessions
628 with varied acquisition parameters⁶⁹. Although each label or imaging modality required
629 retraining, the process was streamlined by the reusable ANTsX infrastructure enabled by
630 rapid adaptation with minimal overhead. These results illustrate the practical benefits of a
631 template-based, low-shot strategy and modular deep learning framework. All trained models,
632 associated training scripts, and supporting resources are openly available and designed for
633 straightforward integration into ANTsX workflows.

634 **Data availability**

635 All data and software used in this work are publicly available. The DevCCF atlas is
636 available at <https://kimlab.io/brain-map/DevCCF/>. ANTsPy, ANTsR, ANTsPyNet, and
637 ANTsRNet are available through GitHub at the ANTsX Ecosystem (<https://github.com/ANTsX>). Training scripts for all deep learning functionality in ANTsXNet can also be found on
638 GitHub (<https://github.com/ntustison/ANTsXNetTraining>). A GitHub repository specifically
639 pertaining to the AllenCCFv3 mapping is available at <https://github.com/dontminchenit/>
640 [CCFAAlignmentToolkit](#). For the other two contributions contained in this work, the longitudinal
641 DevCCF mapping and mouse cortical thickness pipeline, we refer the interested reader to
642 <https://github.com/ntustison/ANTsXMouseBrainMapping>.

⁶⁴⁴ Acknowledgments

⁶⁴⁵ Support for the research reported in this work includes funding from the National Institute
⁶⁴⁶ of Biomedical Imaging and Bioengineering (R01-EB031722) and National Institute of Mental
⁶⁴⁷ Health (RF1-MH124605 and U24-MH114827).

⁶⁴⁸ We also acknowledge the data contribution of Dr. Adam Raikes (GitHub @araikes) of the
⁶⁴⁹ Center for Innovation in Brain Science at the University of Arizona for refining the weights
⁶⁵⁰ of the mouse brain extraction network.

651 **Author contributions**

652 N.T., M.C., and J.G. wrote the main manuscript text and figures. M.C., M.K., R.D., S.S.,
653 Q.W., L.G., J.D., C.G., and J.G. developed the Allen registration pipelines. N.T. and F.K.
654 developed the time-varying velocity transformation model for the DevCCF. N.T. and M.T.
655 developed the brain parcellation and cortical thickness methodology. All authors reviewed
656 the manuscript.

657 **References**

- 658 1. Keller, P. J. & Ahrens, M. B. Visualizing whole-brain activity and development at the
single-cell level using light-sheet microscopy. *Neuron* **85**, 462–83 (2015).
- 659 2. La Manno, G. *et al.* Molecular architecture of the developing mouse brain. *Nature*
596, 92–96 (2021).
- 660 3. Wen, L. *et al.* Single-cell technologies: From research to application. *Innovation
(Camb)* **3**, 100342 (2022).
- 661 4. Oh, S. W. *et al.* A mesoscale connectome of the mouse brain. *Nature* **508**, 207–14
(2014).
- 662 5. Gong, H. *et al.* Continuously tracing brain-wide long-distance axonal projections in
mice at a one-micron voxel resolution. *Neuroimage* **74**, 87–98 (2013).
- 663 6. Li, A. *et al.* Micro-optical sectioning tomography to obtain a high-resolution atlas of
the mouse brain. *Science* **330**, 1404–8 (2010).
- 664 7. Ueda, H. R. *et al.* Tissue clearing and its applications in neuroscience. *Nat Rev
Neurosci* **21**, 61–79 (2020).
- 665 8. Ståhl, P. L. *et al.* Visualization and analysis of gene expression in tissue sections by
spatial transcriptomics. *Science* **353**, 78–82 (2016).
- 666 9. Burgess, D. J. Spatial transcriptomics coming of age. *Nat Rev Genet* **20**, 317 (2019).
- 667 10. Hardwick, S. A. *et al.* Single-nuclei isoform RNA sequencing unlocks barcoded exon
connectivity in frozen brain tissue. *Nature biotechnology* **40**, 1082–1092 (2022).
- 668 11. Hawrylycz, M. *et al.* A guide to the BRAIN initiative cell census network data
ecosystem. *PLoS biology* **21**, e3002133 (2023).
- 669 12. Wang, Q. *et al.* The allen mouse brain common coordinate framework: A 3D reference
atlas. *Cell* **181**, 936–953.e20 (2020).
- 670 13. Perens, J. *et al.* An optimized mouse brain atlas for automated mapping and quantifi-
cation of neuronal activity using iDISCO+ and light sheet fluorescence microscopy.
Neuroinformatics **19**, 433–446 (2021).
- 671 14. Ma, Y. *et al.* A three-dimensional digital atlas database of the adult C57BL/6J mouse
brain by magnetic resonance microscopy. *Neuroscience* **135**, 1203–1215 (2005).

- 672 15. Qu, L. *et al.* Cross-modal coherent registration of whole mouse brains. *Nature Methods* **19**, 111–118 (2022).
- 673 16. Kronman, F. N. *et al.* [Developmental mouse brain common coordinate framework](#). *Nat Commun* **15**, 9072 (2024).
- 674 17. Chuang, N. *et al.* An MRI-based atlas and database of the developing mouse brain. *Neuroimage* **54**, 80–89 (2011).
- 675 18. Dries, R. *et al.* Advances in spatial transcriptomic data analysis. *Genome research* **31**, 1706–1718 (2021).
- 676 19. Ricci, P. *et al.* Removing striping artifacts in light-sheet fluorescence microscopy: A review. *Progress in biophysics and molecular biology* **168**, 52–65 (2022).
- 677 20. Agarwal, N., Xu, X. & Gopi, M. Robust registration of mouse brain slices with severe histological artifacts. in *Proceedings of the tenth indian conference on computer vision, graphics and image processing* 1–8 (2016).
- 678 21. Agarwal, N., Xu, X. & Gopi, M. Automatic detection of histological artifacts in mouse brain slice images. in *Medical computer vision and bayesian and graphical models for biomedical imaging: MICCAI 2016 international workshops, MCV and BAMBI, athens, greece, october 21, 2016, revised selected papers* 8 105–115 (Springer, 2017).
- 679 22. Tward, D. *et al.* 3d mapping of serial histology sections with anomalies using a novel robust deformable registration algorithm. in *International workshop on multimodal brain image analysis* 162–173 (Springer, 2019).
- 680 23. Cahill, L. S. *et al.* Preparation of fixed mouse brains for MRI. *Neuroimage* **60**, 933–939 (2012).
- 681 24. Sunkin, S. M. *et al.* Allen brain atlas: An integrated spatio-temporal portal for exploring the central nervous system. *Nucleic acids research* **41**, D996–D1008 (2012).
- 682 25. Kim, Y. *et al.* Brain-wide maps reveal stereotyped cell-type-based cortical architecture and subcortical sexual dimorphism. *Cell* **171**, 456–469 (2017).
- 683 26. Fürth, D. *et al.* [An interactive framework for whole-brain maps at cellular resolution](#). *Nat Neurosci* **21**, 139–149 (2018).

- 684 27. Li, Y. *et al.* mBrainAligner-web: A web server for cross-modal coherent registration
of whole mouse brains. *Bioinformatics* **38**, 4654–4655 (2022).
- 685 28. Puchades, M. A., Csucs, G., Ledergerber, D., Leergaard, T. B. & Bjaalie, J. G. Spatial
registration of serial microscopic brain images to three-dimensional reference atlases
with the QuickNII tool. *PloS one* **14**, e0216796 (2019).
- 686 29. Eastwood, B. S. *et al.* Whole mouse brain reconstruction and registration to a
reference atlas with standard histochemical processing of coronal sections. *Journal of
Comparative Neurology* **527**, 2170–2178 (2019).
- 687 30. Ni, H. *et al.* A robust image registration interface for large volume brain atlas. *Sci
Rep* **10**, 2139 (2020).
- 688 31. Pallast, N. *et al.* Processing pipeline for atlas-based imaging data analysis of structural
and functional mouse brain MRI (AIDAmri). *Front Neuroinform* **13**, 42 (2019).
- 689 32. Celestine, M., Nadkarni, N. A., Garin, C. M., Bougacha, S. & Dhenain, M. **Sammba-
MRI: A library for processing SmAll-MaMmal BrAin MRI data in python**. *Front
Neuroinform* **14**, 24 (2020).
- 690 33. Ioanas, H.-I., Marks, M., Zerbi, V., Yanik, M. F. & Rudin, M. An optimized registration
workflow and standard geometric space for small animal brain imaging. *Neuroimage*
241, 118386 (2021).
- 691 34. Aggarwal, M., Zhang, J., Miller, M. I., Sidman, R. L. & Mori, S. Magnetic resonance
imaging and micro-computed tomography combined atlas of developing and adult
mouse brains for stereotaxic surgery. *Neuroscience* **162**, 1339–1350 (2009).
- 692 35. Chandrashekhar, V. *et al.* CloudReg: Automatic terabyte-scale cross-modal brain
volume registration. *Nature methods* **18**, 845–846 (2021).
- 693 36. Jin, M. *et al.* SMART: An open-source extension of WholeBrain for intact mouse
brain registration and segmentation. *eNeuro* **9**, (2022).
- 694 37. Negwer, M. *et al.* FriendlyClearMap: An optimized toolkit for mouse brain mapping
and analysis. *Gigascience* **12**, (2022).
- 695 38. Lin, W. *et al.* Whole-brain mapping of histaminergic projections in mouse brain.
Proceedings of the National Academy of Sciences **120**, e2216231120 (2023).

- 696 39. Zhang, M. *et al.* Spatially resolved cell atlas of the mouse primary motor cortex by MERFISH. *Nature* **598**, 137–143 (2021).
- 697 40. Shi, H. *et al.* Spatial atlas of the mouse central nervous system at molecular resolution. *Nature* **622**, 552–561 (2023).
- 698 41. Zhang, Y. *et al.* Reference-based cell type matching of *in situ* image-based spatial transcriptomics data on primary visual cortex of mouse brain. *Scientific Reports* **13**, 9567 (2023).
- 699 42. Klein, S., Staring, M., Murphy, K., Viergever, M. A. & Pluim, J. P. W. [Elastix: A toolbox for intensity-based medical image registration](#). *IEEE Trans Med Imaging* **29**, 196–205 (2010).
- 700 43. Fedorov, A. *et al.* 3D slicer as an image computing platform for the quantitative imaging network. *Magnetic resonance imaging* **30**, 1323–1341 (2012).
- 701 44. Tustison, N. J. *et al.* [The ANTsX ecosystem for quantitative biological and medical imaging](#). *Sci Rep* **11**, 9068 (2021).
- 702 45. Rolfe, S. M., Whikehart, S. M. & Maga, A. M. [Deep learning enabled multi-organ segmentation of mouse embryos](#). *Biol Open* **12**, bio059698 (2023).
- 703 46. Pagani, M., Damiano, M., Galbusera, A., Tsafaris, S. A. & Gozzi, A. Semi-automated registration-based anatomical labelling, voxel based morphometry and cortical thickness mapping of the mouse brain. *Journal of neuroscience methods* **267**, 62–73 (2016).
- 704 47. Anderson, R. J. *et al.* [Small animal multivariate brain analysis \(SAMBA\) - a high throughput pipeline with a validation framework](#). *Neuroinformatics* **17**, 451–472 (2019).
- 705 48. Allan Johnson, G. *et al.* Whole mouse brain connectomics. *Journal of Comparative Neurology* **527**, 2146–2157 (2019).
- 706 49. Yao, Z. *et al.* [A high-resolution transcriptomic and spatial atlas of cell types in the whole mouse brain](#). *Nature* **624**, 317–332 (2023).

- 707 50. Avants, B. B., Epstein, C. L., Grossman, M. & Gee, J. C. [Symmetric diffeomorphic](#)
image registration with cross-correlation: Evaluating automated labeling of elderly
and neurodegenerative brain. *Med Image Anal* **12**, 26–41 (2008).
- 708 51. Tustison, N. J. *et al.* [N4ITK: Improved N3 bias correction](#). *IEEE Trans Med Imaging*
29, 1310–20 (2010).
- 709 52. Bajcsy, R. & Broit, C. Matching of deformed images. in *Sixth International Conference*
on Pattern Recognition (ICPR'82) 351–353 (1982).
- 710 53. Bajcsy, R. & Kovacic, S. [Multiresolution elastic matching](#). *Computer Vision, Graphics,*
and Image Processing **46**, 1–21 (1989).
- 711 54. Gee, J. C., Reivich, M. & Bajcsy, R. [Elastically deforming 3D atlas to match anatomical](#)
[brain images](#). *J Comput Assist Tomogr* **17**, 225–36 (1993).
- 712 55. Klein, A. *et al.* [Evaluation of 14 nonlinear deformation algorithms applied to human](#)
[brain MRI registration](#). *Neuroimage* **46**, 786–802 (2009).
- 713 56. Murphy, K. *et al.* [Evaluation of registration methods on thoracic CT: The EMPIRE10](#)
[challenge](#). *IEEE Trans Med Imaging* **30**, 1901–20 (2011).
- 714 57. Baheti, B. *et al.* [The brain tumor sequence registration challenge: Establishing](#)
correspondence between pre-operative and follow-up MRI scans of diffuse glioma
patients. (2021).
- 715 58. Avants, B. B. *et al.* [The optimal template effect in hippocampus studies of diseased](#)
[populations](#). *Neuroimage* **49**, 2457–66 (2010).
- 716 59. Avants, B. B., Tustison, N. J., Wu, J., Cook, P. A. & Gee, J. C. [An open source](#)
[multivariate framework for n-tissue segmentation with evaluation on public data](#).
Neuroinformatics **9**, 381–400 (2011).
- 717 60. Manjón, J. V., Coupé, P., Martí-Bonmatí, L., Collins, D. L. & Robles, M. [Adaptive](#)
[non-local means denoising of MR images with spatially varying noise levels](#). *J Magn*
Reson Imaging **31**, 192–203 (2010).
- 718 61. Wang, H. *et al.* [Multi-atlas segmentation with joint label fusion](#). *IEEE Trans Pattern*
Anal Mach Intell **35**, 611–23 (2013).

- 719 62. Tustison, N. J. *et al.* Optimal symmetric multimodal templates and concatenated random forests for supervised brain tumor segmentation (simplified) with *ANTsR*. *Neuroinformatics* (2014) doi:10.1007/s12021-014-9245-2.
- 720 63. Tustison, N. J., Yang, Y. & Salerno, M. Advanced normalization tools for cardiac motion correction. in *Statistical atlases and computational models of the heart - imaging and modelling challenges* (eds. Camara, O. et al.) vol. 8896 3–12 (Springer International Publishing, 2015).
- 721 64. McCormick, M., Liu, X., Jomier, J., Marion, C. & Ibanez, L. ITK: Enabling reproducible research and open science. *Front Neuroinform* **8**, 13 (2014).
- 722 65. Beg, M. F., Miller, M. I., Trouvé, A. & Younes, L. Computing large deformation metric mappings via geodesic flows of diffeomorphisms. *International Journal of Computer Vision* **61**, 139–157 (2005).
- 723 66. Tustison, N. J. & Avants, B. B. Explicit B-spline regularization in diffeomorphic image registration. *Front Neuroinform* **7**, 39 (2013).
- 724 67. Hsu, L.-M. *et al.* CAMRI mouse brain MRI data.
- 725 68. Reshetnikov, V. *et al.* High-resolution MRI data of brain C57BL/6 and BTBR mice in three different anatomical views.
- 726 69. Rahman, N., Xu, K., Budde, M. D., Brown, A. & Baron, C. A. A longitudinal microstructural MRI dataset in healthy C57Bl/6 mice at 9.4 tesla. *Sci Data* **10**, 94 (2023).
- 727 70. Liu, J. *et al.* Concordance of MERFISH spatial transcriptomics with bulk and single-cell RNA sequencing. *Life Sci Alliance* **6**, (2023).
- 728 71. Stringer, C., Wang, T., Michaelos, M. & Pachitariu, M. Cellpose: A generalist algorithm for cellular segmentation. *Nat Methods* **18**, 100–106 (2021).
- 729 72. Jia, H., Yap, P.-T., Wu, G., Wang, Q. & Shen, D. Intermediate templates guided groupwise registration of diffusion tensor images. *NeuroImage* **54**, 928–939 (2011).
- 730 73. Tang, S., Fan, Y., Wu, G., Kim, M. & Shen, D. RABBIT: Rapid alignment of brains by building intermediate templates. *NeuroImage* **47**, 1277–1287 (2009).

- 731 74. Dewey, B. E., Carass, A., Blitz, A. M. & Prince, J. L. Efficient multi-atlas registration
using an intermediate template image. in *Proceedings of SPIE—the international society
for optical engineering* vol. 10137 (NIH Public Access, 2017).
- 732 75. Perens, J. *et al.* Multimodal 3D mouse brain atlas framework with the skull-derived
coordinate system. *Neuroinformatics* **21**, 269–286 (2023).
- 733 76. Gong, H. *et al.* High-throughput dual-colour precision imaging for brain-wide connec-
tome with cytoarchitectonic landmarks at the cellular level. *Nat Commun* **7**, 12142
(2016).
- 734 77. Wang, J. *et al.* Divergent projection patterns revealed by reconstruction of individual
neurons in orbitofrontal cortex. *Neurosci Bull* **37**, 461–477 (2021).
- 735 78. Rotolo, T., Smallwood, P. M., Williams, J. & Nathans, J. Genetically-directed, cell
type-specific sparse labeling for the analysis of neuronal morphology. *PLoS One* **3**,
e4099 (2008).
- 736 79. Peng, H. *et al.* Morphological diversity of single neurons in molecularly defined cell
types. *Nature* **598**, 174–181 (2021).
- 737 80. Kronman, F. A. *et al.* Developmental mouse brain common coordinate framework.
bioRxiv (2023) doi:[10.1101/2023.09.14.557789](https://doi.org/10.1101/2023.09.14.557789).
- 738 81. Chon, U., Vanselow, D. J., Cheng, K. C. & Kim, Y. Enhanced and unified anatomical
labeling for a common mouse brain atlas. *Nat Commun* **10**, 5067 (2019).
- 739 82. Tasic, B. *et al.* Adult mouse cortical cell taxonomy revealed by single cell transcript-
omics. *Nat Neurosci* **19**, 335–46 (2016).
- 740 83. Bergmann, E., Gofman, X., Kavushansky, A. & Kahn, I. Individual variability in
functional connectivity architecture of the mouse brain. *Commun Biol* **3**, 738 (2020).
- 741 84. Billot, B. *et al.* SynthSeg: Segmentation of brain MRI scans of any contrast and
resolution without retraining. *Med Image Anal* **86**, 102789 (2023).
- 742 85. Tustison, N. J. & Amini, A. A. Biventricular myocardial strains via nonrigid registration
of anatomical NURBS model [corrected]. *IEEE Trans Med Imaging* **25**, 94–112 (2006).
- 743 86. Avants, B. B. *et al.* The Insight ToolKit image registration framework. *Front Neu-
roinform* **8**, 44 (2014).

- ⁷⁴⁴ 87. Falk, T. *et al.* U-net: Deep learning for cell counting, detection, and morphometry. *Nat Methods* **16**, 67–70 (2019).
- ⁷⁴⁵ 88. Tustison, N. J. *et al.* Image- versus histogram-based considerations in semantic segmentation of pulmonary hyperpolarized gas images. *Magn Reson Med* **86**, 2822–2836 (2021).